Title

Fractured rock hydromechanics: From borehole testing to solute transport and CO2 storage

Authors

Tsang, Y.
Rutqvist, J.

Publication Date

2007

Fractured Rock Hydromechanics: From Borehole Testing to Solute Transport and CO_2 Storage

Chin-Fu Tsang,[1] Jonny Rutqvist,[1] and Ki-Bok Min[2]

[1]Earth Sciences Division
1 Cyclotron Road, Lawrence Berkeley National Berkeley
Berkeley, California 94720, USA

[2]Department of Energy and Geo-Environmental Engineering
Pennsylvania State University
University Park, Pennsylvania, 16802, USA

Contact: Chin-Fu Tsang, cftsang@lbl.gov

6640 words, 23 figures, 32 references

Running Title: Fractured Rock Hydromechanics

Abstract: The interaction between mechanical deformation and fluid flow in fractured rock gives rise to a host of coupled hydromechanical processes, which form the basis of a number of interesting research questions with practical implications. This paper will first discuss these processes in general, describing two numerical models that have been developed to analyze these processes. Then, four very different studies will be presented to illustrate the richness of this field. The first study has to do with borehole injection testing to determine fracture parameters and how hydromechanical effects will modify test results. The second study is on stress changes (caused by stress release) in rock near a tunnel during excavation, causing significant changes in fluid pressures in the region. The third study is on the relationship between mechanical effects and flow anisotropy and channeling in a rock block with a fracture network. The fourth study pertains to the hydromechanical effects associated with deep CO_2 injection and storage. These examples serve to demonstrate the various interesting research problems in fractured rock hydromechanics. In the coming years, we expect intensified activity and further advances in this exciting field of research.

Introduction

Hydromechanical coupling in fractured rock masses is an important issue for many rock mechanics and hydrogeology applications (Rutqvist & Stephansson 2003). Fractured rock masses are composed of continuum rock matrix with embedded fractures, and the latter act as the main pathways of fluid flow. Hydromechanical coupling can be direct or indirect (Rutqvist & Stephansson 2003). A direct coupling occurs when applied stresses produce a change in hydraulic pressure, or vice versa. An indirect coupling occurs when mechanical changes affect hydraulic property parameters, or when hydraulic conditions affect mechanical properties. For example, apertures of fractures can change as a result of normal stress-induced closures or openings, and also as result of shear stress-induced dilations. Hence, the permeability of fractured rock masses, which is strongly dependent on fracture apertures, is stress dependent. The indirect coupling is particularly important, since stress-induced changes in permeability can be large (several orders of magnitude) and irreversible under perturbations resulting from various natural and human activities. These activities include underground construction, causing stress redistributions close to rock openings, as well as geothermal energy and oil/gas reservoir productions, where injection and extraction of fluids entail significant changes in fluid pressures and effective stresses underground.

In the early and mid-1980s, coupled processes associated with nuclear waste repositories were discussed in a series of workshops, concluded with an edited book on the subject (Tsang 1987). More general discussions on coupled processes in geologic systems were given by Tsang (1991, 1999). Numerical models capable of simulating coupled thermo-hydro-mechanical processes in fractured rock masses have been in existence since the early 1980s. However, it is only in the last few years that models capable of simulating coupled thermo-hydro-mechanical processes under multiphase flow conditions (such as those of unsaturated geologic formations) have come into being. Reviews of state-of-the-art numerical methods and modeling were presented by Jing & Hudson (2002), and Rutqvist *et al.* (2001).

In the next section, we shall describe two numerical simulators, the ROCMAS and TOUGH-FLAC codes, which are used in the studies presented in this paper. They also serve to provide some insight into the complexity needed for coupling hydrologic or rock mechanics models. Following this, four very different studies of coupled hydromechanical processes are presented.

1. Hydromechanical effects in injection well testing, a field and modeling study of indirect coupling, involving one fracture intercepted by a well;
2. Hydromechanical effects in tunnel drilling, a field and modeling study of direct coupling in rock mass around a tunnel under excavation, involving effects of stress release and redistribution;
3. Hydromechanical effects on flow in fracture networks, a modeling study of indirect coupling in rock mass, involving many fractures in a network;
4. Hydromechanical effects in CO_2 injection and storage, a modeling study of direct coupling in rock mass, involving potential fracture opening under injection and buoyancy pressures in a multiphase system.

Some brief remarks will conclude the paper.

Two Numerical Simulators for Modeling Coupled Hydromechanical Processes

The first simulator is the ROCMAS code (ROCk Mass Analysis Scheme), a finite-element code for analysis of coupled thermal-hydrological-mechanical (THM) processes in saturated-unsaturated

fractured porous media. It has been gradually developed and extended since the early 1980s by J. Noorishad and coworkers. A hydromechanical formulation for fractured rock, based on Biot's general effective stress theory (Biot 1941), was developed (Noorishad *et al.* 1982) and then extended to nonisothermal conditions (Noorishad *et al.* 1984, 1992).

Noorishad and Tsang (1996) and Rutqvist *et al.* (2001) extended the original formulation of coupled thermohydroelasticity in terms of Biot's theory of consolidation to partially saturated media through Philip and de Vries' theory for heat and moisture flow in soil. In this theory, the three phases, solid, liquid, and gas, are present. However, it is assumed that the gas pressure P_g is constant and equal to atmospheric pressure throughout the porous medium. Vapor transport occurs only through molecular diffusion driven by a gradient in vapor concentration (density), while advection of vapor with bulk gas flow is neglected. As in the general case, the vapor density in the medium is governed by Kelvin's relation, which assumes thermodynamic equilibrium for pore liquid in contact with its vapor, with phase changes occurring as evaporation-condensation processes.

The second simulator is the TOUGH-FLAC code (Rutqvist *et al.* 2002), based on a coupling of the two existing computer codes TOUGH2 (Pruess *et al.* 1999) and FLAC3D (Itasca Consulting Group 1997). TOUGH2 is a well-established simulator for geohydrological analysis with multiphase, multicomponent fluid flow and heat transport, while FLAC3D is a widely used commercial code designed for rock and soil mechanics. For analysis of coupled THM problems, the TOUGH2 and FLAC3D are executed on compatible numerical grids and linked through external coupling modules, which serve to pass relevant information between the field equations solved in the respective codes (Fig. 1). A TOUGH-to-FLAC link takes multiphase pressures, saturation, and temperature from the TOUGH2 simulation and provides the updated temperature and pore-pressure information to FLAC3D (Fig. 1). Because the TOUGH2 mesh uses one gridpoint within each element, and FLAC3D nodes are located in element corners, data have to be interpolated from mid-element (TOUGH2) to corner locations (FLAC3D).

After data transfer, FLAC3D internally calculates thermal expansion and effective stress according to:

$$\Delta\boldsymbol{\varepsilon}^{T} = \mathbf{I}\beta_T \Delta T \tag{1}$$

$$\boldsymbol{\sigma}' = \boldsymbol{\sigma} - \mathbf{I}\alpha P \tag{2}$$

where $\boldsymbol{\varepsilon}^{\mathbf{T}}$ is thermal strain, β_T is the linear thermal expansion coefficient, $\mathbf{I}$ is the unit tensor, T is temperature, $\boldsymbol{\sigma}'$ is effective stress, $\boldsymbol{\sigma}$ is total stress, α is the Biot effective stress parameter, and P is pore fluid pressure. In a multiphase flow calculation, the value of P transferred to FLAC3D could represent an average pore pressure calculated from the pressures of the various phases (Rutqvist *et al.* 2002).

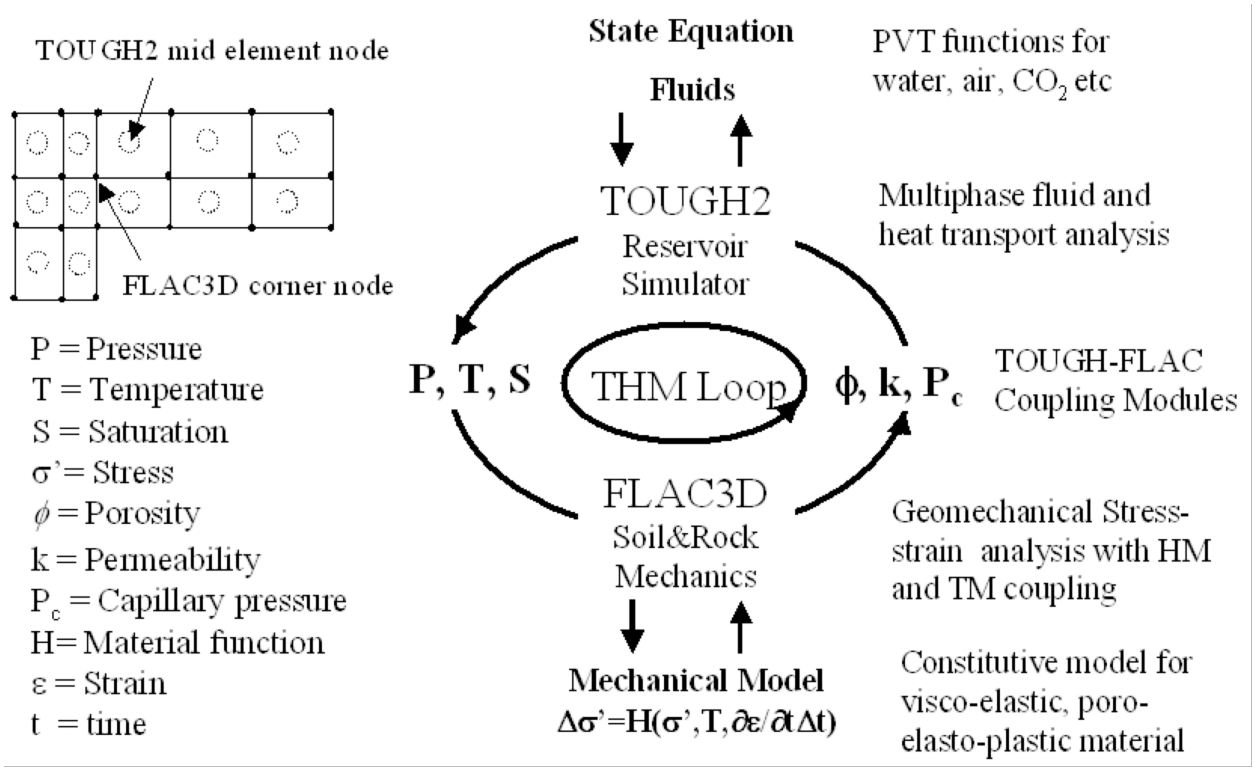

Fig. 1. TOUGH-FLAC simulator coupled THM analysis with multiphase fluid flow

A FLAC-to-TOUGH link takes the element stress and deformation from FLAC3D and updates the corresponding element porosity, permeability, and capillary pressure to be used by TOUGH2, according to the following general expressions:

$$\phi = \phi(\acute{o}, å) \tag{3}$$

$$\mathbf{k} = \mathbf{k}(\acute{o}, å) \tag{4}$$

$$P_c = P_c(\acute{o}, å) \tag{5}$$

No interpolation in space is required for this data transfer because stress and strain are defined in FLAC3D elements, which are identical to TOUGH2 elements. A TOUGH-FLAC coupling module for this link would then calculate the hydraulic property changes, based on material-specific theoretical or empirical functions.

A separate batch program controls the coupling and execution of TOUGH2 and FLAC3D for the linked TOUGH-FLAC simulator. It was done within the FLAC3D input file using the FLAC-FISH programming language (Itasca Consulting Group 1997). The calculation is then stepped forward with the transient TH analysis in TOUGH2, by conducting, at each time step or at the TOUGH2 Newton iteration level, a quasi-static mechanical analysis with FLAC3D, to calculate stress-induced changes in porosity and intrinsic permeability. By limiting to cases with small strain conditions, there is no change in mesh dimension during the simulations.

Hydromechanical Effects in Injection Well Testing

In this study, *in situ* hydromechanical properties (Fig. 2) were determined on fractures intersecting a 1700 m deep borehole, KLX02, at the Laxemar area near Äspö Hard Rock Laboratory in Sweden (Rutqvist *et al.* 1997). The fractures were located at three highly conductive zones at depths of 270, 315, and 340 m. The hydromechanical properties were back-calculated by coupled numerical modeling of single-borehole multiple-pressure injections tests.

The KLX02 borehole is cased to 200 m depth and has a diameter of 76 mm for depth greater than 200 m. The bedrock consists mainly of granite and diorite, and the fracture frequency is in general low, especially down to 700 m and between 1100–1500 m. The three test zones could be identified from flow, temperature, and electrical resistivity logging as the most hydraulic conductive zones in the upper 700 m of the borehole (Ekman 1997). The zones at 270 and 340 m coincide with the intersection of fracture zones a few meters wide, which also were identified by borehole radar. The rock in these zones was reported to be crushed and fractured granite, with a frequency of 10 to 20 fractures per meter. Pulse-injection tests, together with images from a high-resolution TV system, showed that the transmissivity in each zone was dominated by flow through a few open fractures. The most hydraulic conducting fractures appear to have very rough surfaces with open channels between contact points and parts filled or coated with calcite or chlorite. The orientation of the fractures at 270 and 340 m are oblique to the fracture zone and may be strike-slip shear fractures. In discussions below, we shall exclusively describe the study of the fracture zone at 270 m.

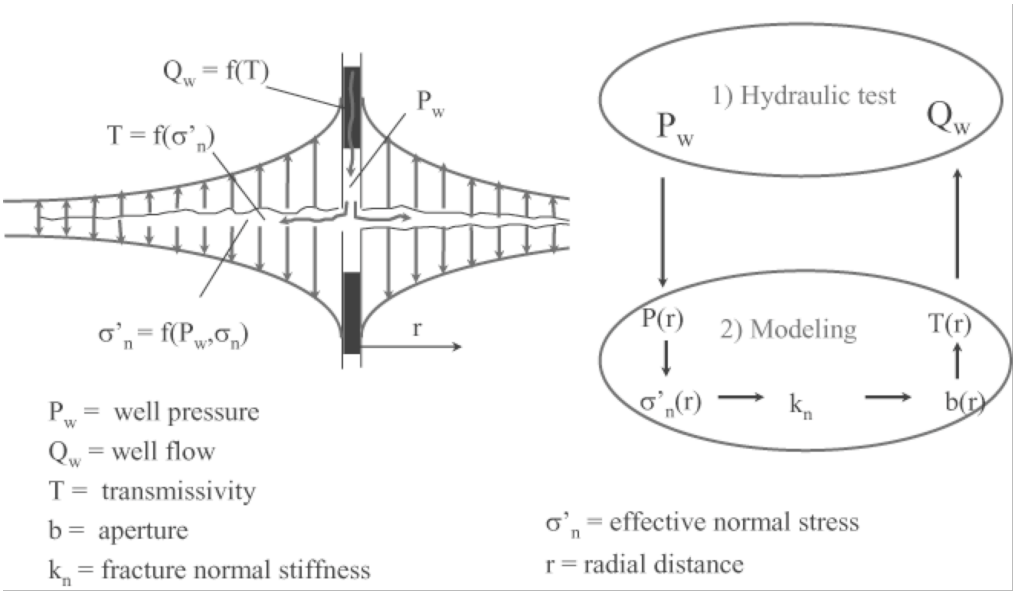

Fig. 2. *In situ* determination of hydromechanical properties of rock joints

During injection well testing, the fracture of interest is isolated in the well by the use of one packer above and another one below the section with the fracture. An increase in pressure P_w in the packered interval will be accompanied by an increase in flow rate Q_w (Fig. 2). Through modeling, in this case using the ROCMAS code, the pressure profile P(r) in the fracture, as a function of radial distance from the well, can be calculated from P_w. The effective normal stress σ_n' is then calculated using P(r), and the corresponding fracture aperture changes b(r) are evaluated if one assumes a fracture normal stiffness k_n. Transmissivity T of the fracture is calculated from b(r) and provides the parameter needed to obtain injection flow rate, which can be compared with the measured Q_w.

Parameters are adjusted to ensure a good match between simulated and measured data, thus yielding their optimal values.

Below, we shall consider the use of the hydraulic jacking test, which is conducted by a step-wise increase of the fluid pressure. At each step, the well pressure is kept constant for a few minutes until the flow is steady (Fig. 3). The technique was first applied by Londe & Sabarly (1966) and Louis *et al.* (1977) to study pressure-sensitive permeability under dam foundations. Rutqvist (1995) and Rutqvist *et al.* (1997) used hydraulic jacking tests, combined with coupled numerical modeling, for determining the *in situ* hydromechanical (HM) properties of fractures in crystalline rock. The numerical analysis of these injection tests shows that the flow rate at each pressure step is strongly dependent on the fracture aperture and normal stiffness of the fracture in the vicinity of the borehole, where the pressure changes the most (Fig. 4). Fig. 5 shows field-test results for the successive pressure at each step against the flow rate attained at that step, in the case of the fracture intercepted by the Laxemar KLX02 borehole at 270 m depth (Rutqvist *et al.* 1997). At the early part of the step-wise increasing pressure, the flow rate increases as a nonlinear function of pressure. A temporal peak-pressure is obtained at a flow rate of 1.3 liters/minute before the pressure begins to decrease with an increasing flow rate. A shear-slip analysis of the particular fracture, which was inclined to the principal *in situ* stresses, indicated that these irreversible fracture responses could be caused by shear slip, as the fluid pressure reduced the shear strength of the fracture. The subsequent step-down of pressures took a different path because of the change in hydromechanical properties resulting from shearing and fracturing.

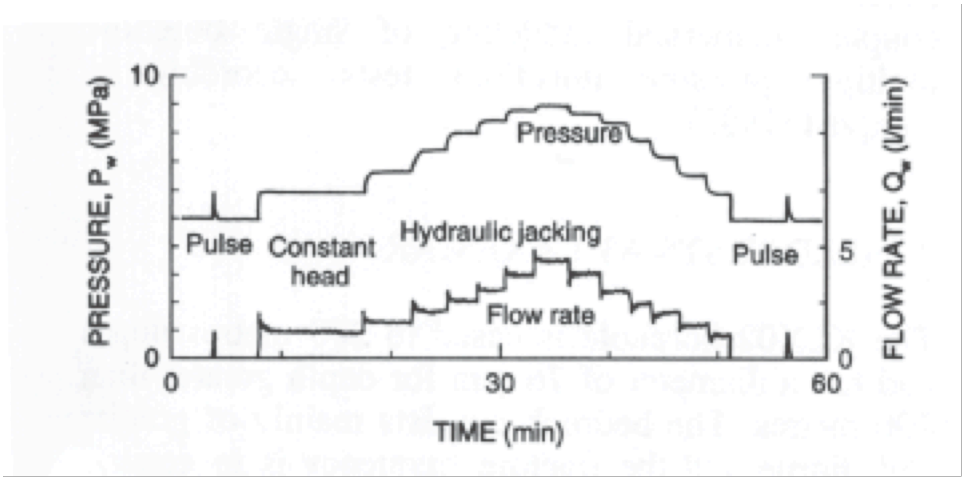

Fig. 3. Hydraulic jacking test: pressure and flow-rate data

The overall results from the hydraulic jacking tests conducted at Laxemar showed that the pressure sensitivity of the fractures is strongly dependent on the initial hydraulic permeability. The permeability of the most conductive fractures is relatively insensitive to injection pressure, whereas the permeability of the least conductive fractures can be strongly dependent on the injection pressure. From the borehole-televiewer image, the most conductive fractures appear to be open fractures that are incompletely cemented, indicating flow channels in a fracture that are "locked open" by shear dislocation or mineral filling (Rutqvist *et al.* 1997).

As an additional remark, one notes that if a pulse injection test, instead of the hydraulic-jacking test, is made on the fracture (see first peak at about 4 minutes in Fig. 3), the pressure increase P(r) is very much limited to a small area around the well (Fig. 4). In this case, the induced changes in σ_n', b(r), and fracture transmissivity are also very small. Thus, the coupled hydromechanical effect is expected not to be significant, so that a conventional hydrological analysis method would apply. This

observation presents the interesting possibility that a hydraulic jacking test and pulse injection test combined, on the same fracture, could be analyzed simultaneously to optimally determine the fracture hydraulic and mechanical parameters.

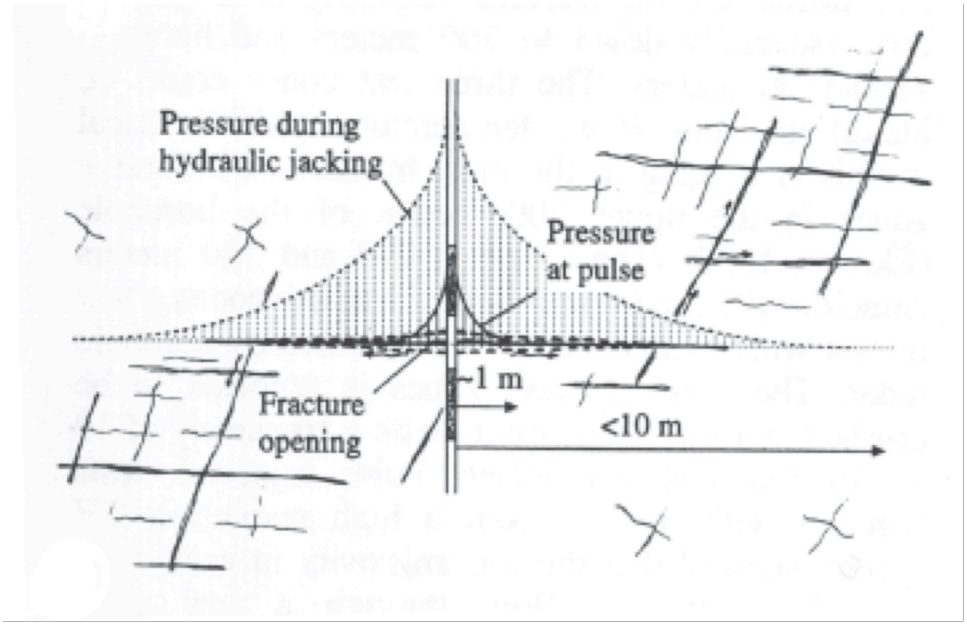

Fig. 4. Schematic picture of pressure profiles in a fractured rock during a hydraulic jacking test and a pulse injection test

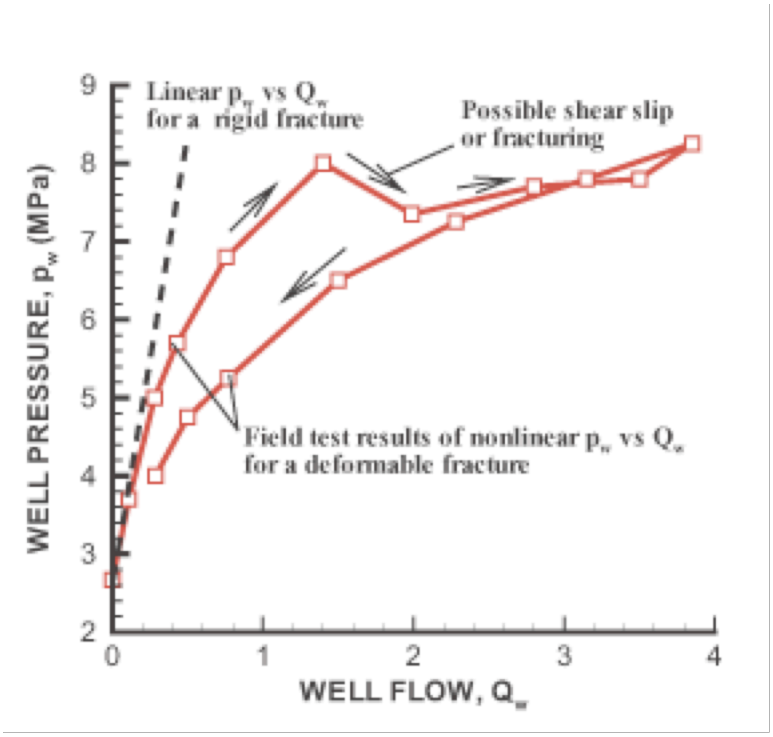

Fig. 5. Numerical modeling and field experiment data for a hydraulic-jacking test involving increasing and then decreasing pressure steps. For comparison, the expected result for a rigid fracture is shown as the broken line.

Hydromechanical Effects During Tunnel Drilling

During the excavation of the FEBEX Tunnel, located in fractured crystalline rock at the Grimsel Test Site in Switzerland, peculiar responses in fluid pressure were observed in the surrounding rocks (McKinley *et al.* 1996). A borehole was first drilled at 3 m away from and parallel to a planned tunnel and then packered into two 10-m sections, P3 and P4. During tunnel drilling using a tunnel boring machine (TBM), the water pressures in P3 and P4 were monitored. Fig. 6 shows the drilling and resting cycles of the TBM (the line indicated by the shaded area) and the P3 and P4 pressure responses. The front end of the tunnel passed P4, but just reached P3. Thus, the pressure behavior in P3 was not as clear as one would expect, but the P4 pressure showed a distinct response, with two peaks corresponding to two drilling-and-resting cycles (Fig. 6). It is believed that during tunnel drilling directly across from P4 interval, the pore pressure in P4 increased because of the induced stress concentration near P4. Then, during the resting period between drilling, water leaked away because of rock permeability, and thus the pore pressure decreased (Fig. 2).

To understand the data, a fully coupled three-dimensional HM modeling of the tunnel-drilling procedure was performed (Rutqvist *et al.* 2004) using the finite element code ROCMAS (Rutqvist *et al.* 2001). The mesh used for the simulation is shown in Fig. 7. An initial stress field was assigned according to the range of stress measurements in the Grimsel area (Pahl *et al.* 1989): σv=10 MPa, σh=15 MPa and σH=30 MPa, where σH is oriented 45º from the tunnel axis.

The FEBEX tunnel was modeled according to the actual TBM schedule. The boring was conducted in ten-hour shifts, with no activities during nights and weekends, and, in the modeling, uniform excavation during each ten-hour shift is assumed. Fig. 8 presents the simulated changes in mean stress at 18:00 on October 25 (See Fig. 6, when excavation is at 61 m directly opposite zone P4.) Fig. 9 shows the corresponding fluid pressure, with two zones of increased values, one around the front-left side of the excavation and one above it, near its front. Fig. 8 shows that near these two zones of pressure increase, the mean stress has increased as a result of the excavation. In contrast, the fluid pressure on the side of the drift is decreased where the mean stress has decreased. The figures also show that the HM-induced changes in fluid pressures are temporal. For example, the HM-induced fluid-pressure rise above the tunnel diminishes 5 to 10 m behind the tunnel face, because of drainage into the tunnel.

Fig. 10 presents the predicted and measured pressure responses in P4. While the timing of pressure response is about right, the predicted values are opposite to what were measured, i.e., pressure drops instead of peaks. The reason behind the discrepancy was found in the assumed *in situ* stress field, which is an important factor that controls the fluid-pressure changes. It was found in a variation study that the measured pressure changes can be reproduced by changing the orientation and magnitude of the stress field. An example of a much-improved match is shown in Fig. 11, together with the adjusted stress field shown in the upper-right corner. The main point of this example is to show the high sensitivity of pore-pressure changes to local *in situ* stress fields. It was shown in a more general study that the measured pressure responses can be captured if the stress field is rotated such that contraction (compressive strain rate) and corresponding increases in mean stress occur near the P4 borehole on the side of the drift. Good agreement between measured and simulated evolution of fluid pressure could be obtained if the maximum principal stress were rotated about 40° from the horizontal. Such a rotation of the local *in situ* stress field is not unrealistic, especially considering the presence of the Lamprophyre zones and other geological features.

Thus, one conclusion from the study is that significant pore-pressure responses can be expected in the rock during tunnel excavation, and these responses are very sensitive to the local stress field. The local stress field could well be different from the regional stress field, especially if there is a major fault zone or other geological features in the vicinity of the tunnel. Perhaps the study described in this section suggests a way to study the local stress field.

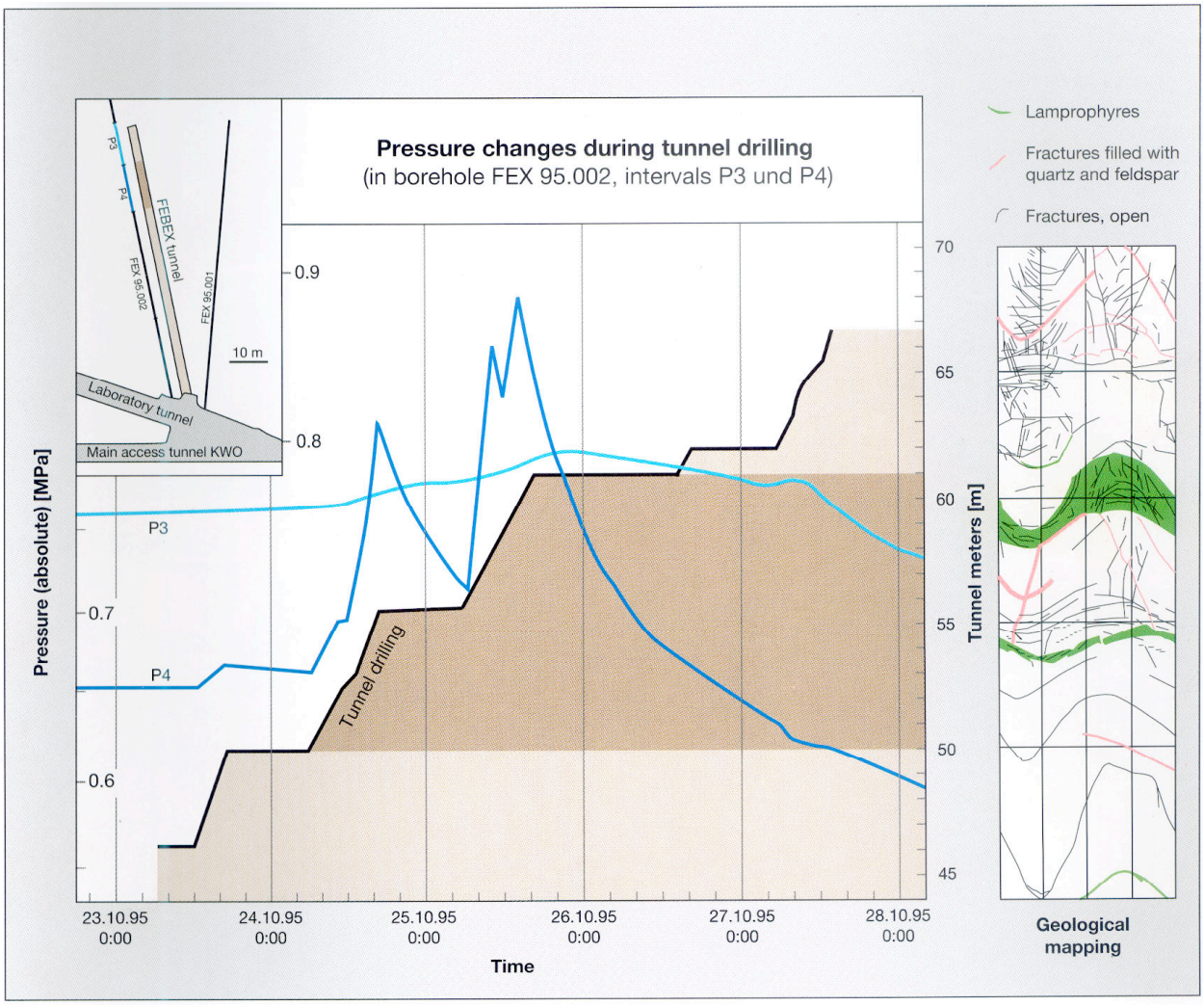

Fig. 6. During TBM excavation of the FEBEX tunnel, distinct increases in fluid pressure were observed in a borehole interval (P4) located a few meters away from the drift wall (from McKinley *et al.* 1996).

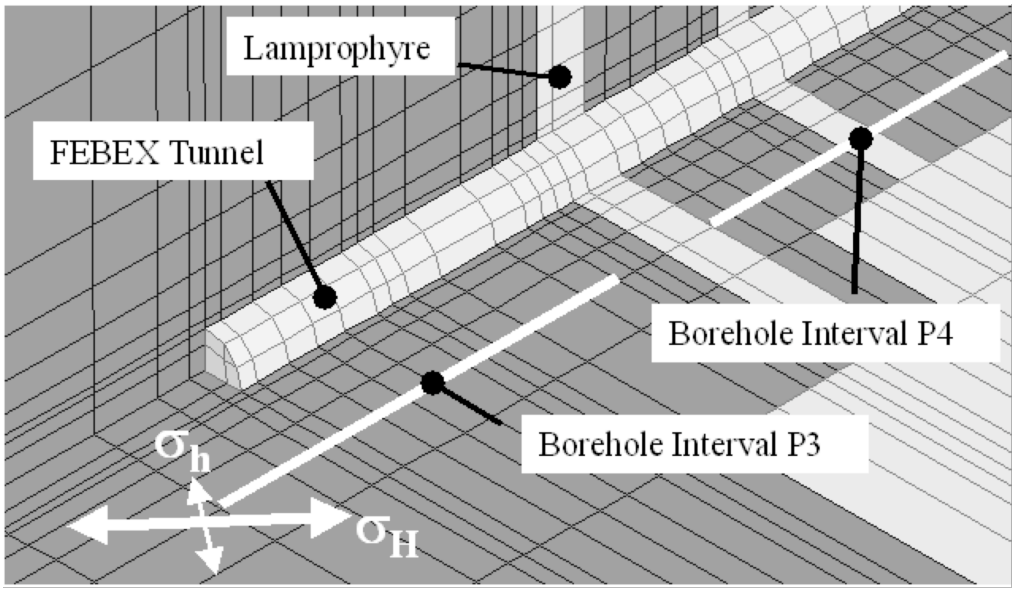

Fig. 7. Mesh design for simulating stress and pore-pressure changes around the FEBEX tunnel

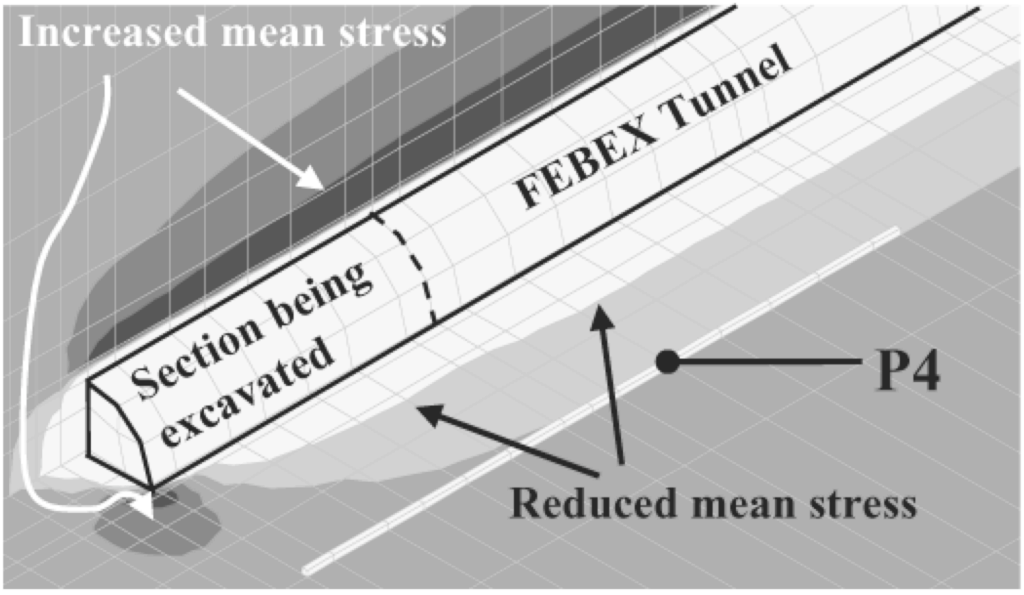

Fig. 8. Calculated changes in mean stress at the end of the second step of excavating the FEBEX tunnel (see Fig. 6, 61 m on the right axis)

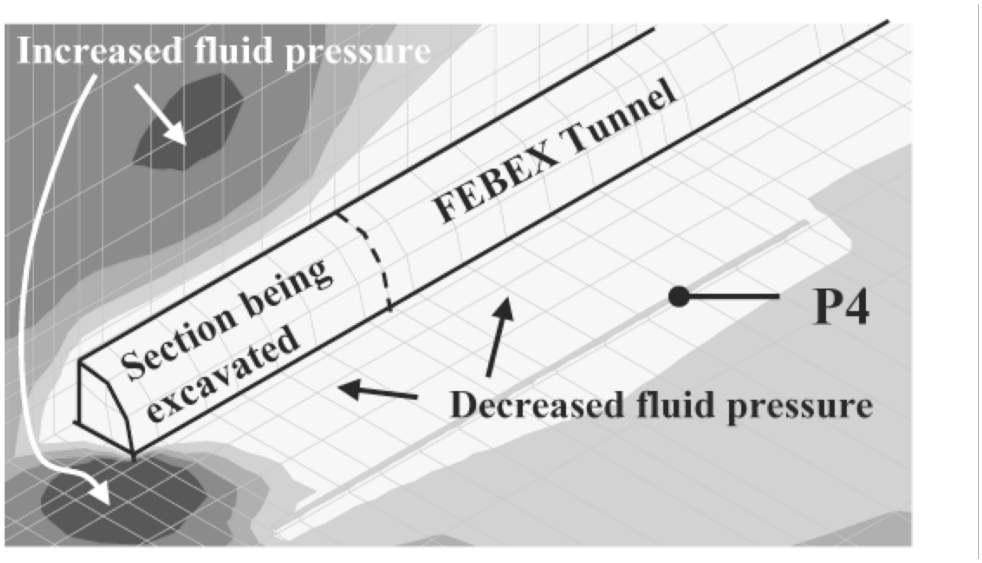

Fig. 9. Calculated change in pore pressure at the end of the second step in excavating the FEBEX tunnel (see Fig. 6, 61 m on the right axis)

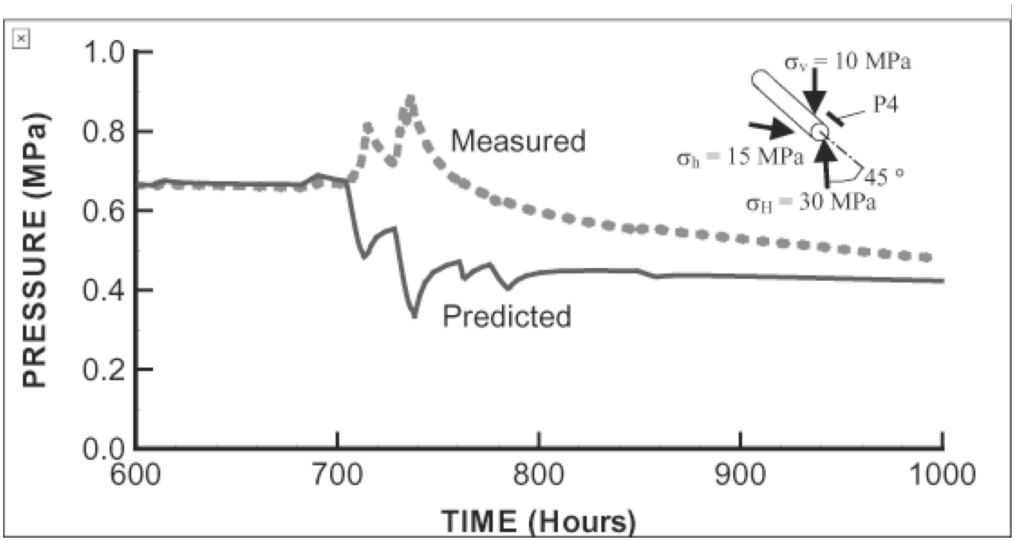

Fig. 10. Predicted and measured pore-pressure evolution for the estimated regional stress field

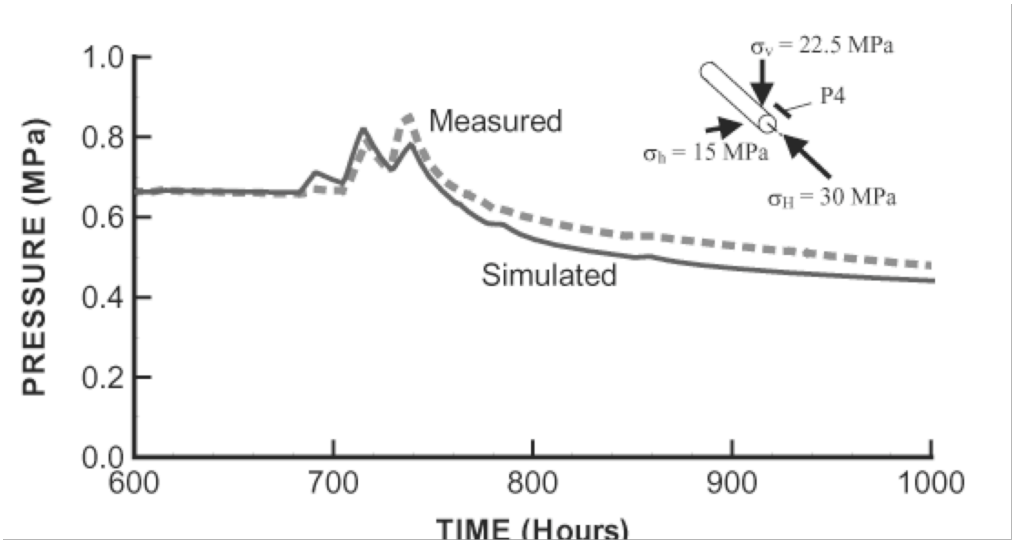

Fig. 11. Simulated and measured pore-pressure evolution for the adjusted local stress field

Hydromechanical Effects on Flow in Fracture Networks

The objective of the study is to investigate the stress-dependent permeability in fractured rock masses considering a realistic representation of a fracture-network system and stress-deformation behavior. The geometrical basis for this study is a discrete fracture network (DFN) generated in a square region, 5 m by 5 m in size (Fig. 12), based on statistical information of fractures from a site characterization program at Sellafield, England (Andersson & Knight 2000). The size of 5 m × 5 m is selected for the model, based on previous investigations for the calculations of the equivalent mechanical and hydraulic properties. This scale was shown (Min *et al.* 2003; Min & Jing 2003) to represent both the initial mechanical and hydraulic REVs (Representative Elementary Volumes).

After the generation of the DFN model, various boundary stresses σ_x and σ_y were applied to generate deformed models for flow analysis (Fig. 13). Each rock block in between fractures was modeled as continuous, homogeneous, isotropic, linear, elastic, and impermeable media. The application of σ_x and σ_y is carried out in two ways. The first is to keep their ratio the same at $\sigma_x/\sigma_y = 1.3$. The second is to keep σ_y constant at 5.0 MPa and vary σ_x, so that their ratio ranges from 0.5 to 5.0. For each case, after the mechanical calculations are completed and the aperture value of each fracture is revised, flows in x and y direction are calculated by applying a pressure step in the x and y direction, respectively. From the calculated flows, the permeabilities of the fracture network in the two directions are then calculated as k_x and k_y.

Key factors affecting the hydraulic behavior of fractures, such as opening, closing, sliding and dilation, were modeled by incorporating relevant fracture constitutive models. A step-wise nonlinear normal stress-normal closure relation is adopted to approximate a hyperbolic normal deformation process. The stress-shear displacement fracture behavior was modeled by an elasto-perfectly plastic constitutive model, with a Mohr–Coulomb failure criterion and fracture dilation occurs when it starts to slide. This dilation continues until a predefined critical shear displacement (Ucs) value, beyond which the dilation stops (Min *et al.* 2004).

Fig. 14 shows the aperture changes with the increase of both horizontal and vertical boundary stresses while keeping a constant stress ratio of 1.3 between them. Because the stress ratio is close to

unity, the stress states in most of the fractures do not cause shear failure, and normal stress is the main cause for the aperture change, basically closure. The initial aperture (30 mm) at a zero stress level decreased to 8.8 mm (mean values) when the mean stress magnitude was increased to 23 MPa. The changes in fracture apertures occur almost uniformly within the model region with the increase of stresses. This is because the fracture-normal closure resulting from normal stress increases is the dominating mechanism that controls fracture deformation, since significant shear dilation does not occur with the stress ratio equal to 1.3. Aperture anomalies can be observed in a few isolated places in the model region, mainly in the sharp corners of the blocks where fracture failure occurs as a result of stress concentration. However, these were observed only locally, without being extended to entire fracture length, and therefore their influence on the overall fluid flow field is minor for this two-dimensional analysis.

Fig. 15 shows the aperture changes when the horizontal boundary stress is increased in steps from 2.5 to 25 MPa, with a fixed vertical boundary stress of 5 MPa (the k ratio changing from 0.5 to 5), to investigate the influence of shear failure in fractures induced by larger differential stresses. In contrast to Fig. 14, fracture aperture changes are not uniform. At the stress ratio of 3.0, large apertures can be observed in the critically oriented and well-connected fractures, thus affecting the flow paths significantly. This tendency becomes increasingly clear at the stress ratio of 5. An examination of the results suggests the following reasons for this phenomenon:

- Critically oriented fractures continue to dilate under increasing differential stresses, which leads to much larger apertures of these fractures compared to their less critically oriented neighboring fractures. The critical orientation is the orientation that is prone to shear failure due to applied stresses: it is calculated to be about 33° (Min *et al.* 2004) in our example.
- It is not only the orientation of fractures, but also the connectivity of fractures that is needed for the formation of sufficient fracture dilation by stress change. Because the neighboring fractures can hinder further plastic shear development in fractures of critical orientation, many critically oriented fractures with poor connectivity could not produce large apertures, due to their poor connection to the fractures with similar orientation.
- The trace length of fractures is another important factor in forming clustered fractures conducting fluid flow with large apertures. This is natural with respect to connectivity, since longer fractures have a higher degree of connectivity compared to short ones, which are prone to being hindered by the neighboring fractures and rock blocks. The figure shows that the long fractures are much more dilated than the shorter fractures (among the critically oriented fractures), which is also in line with field observations (e.g., Renshaw & Park 1997).

Fig. 16 presents the calculated equivalent-permeability changes with the increasing stress ratio. To evaluate the effect of shear dilation, the results with a pure elastic fracture model that excludes failure and dilation are shown as dashed lines in Fig. 16. The pure elastic and the elastoplastic models show a similar response until the stress ratio k reaches approximately 2.5, which is the starting point of shear failure for fractures inclined at about 33° from the horizontal plane. At this point and afterwards, some fractures in the fractured rock masses start to fail and, with continued shear dilation, notable differences between the models are observed. At stress ratio of 5, the additional contribution from shear dilations of fractures is more than one order of magnitude for k_x and a factor of four for k_y. On the other hand, the fractures that are not critically oriented continue to close with an increase in stresses, and this makes their apertures smaller and fluid flow reduced. However, the dilation of fractures caused by shear is abrupt (with larger gradients) when shear failure starts to develop, and this dominates the process. As the horizontal boundary stress σ_x increases, the range of fracture orientation angles for possible shear failure also increases, with resulting increased permeability. The increase of permeability stabilizes after a certain stress ratio,

because the shear dilation of a fracture does not continue after the critical shear displacement is reached. Interestingly, this increased permeability is analogous to experimental results on the intact rocks, which show a similar decrease and increase in permeability with increasing differential stresses (Lee & Chang 1995).

Fig. 17 shows the normalized flow rates in each fracture intersecting the left vertical boundary of the model. The initial uniform flow pattern changes when fracture dilation starts to develop, at a stress ratio of about 3 and beyond. Only 10% of fractures (four out of 40 fractures) carry about 50% and 70% of the fluid flow across the boundary, at a stress ratio of 3 and 5, respectively—which demonstrates the channeling effect induced by stresses. This is a very dramatic effect.

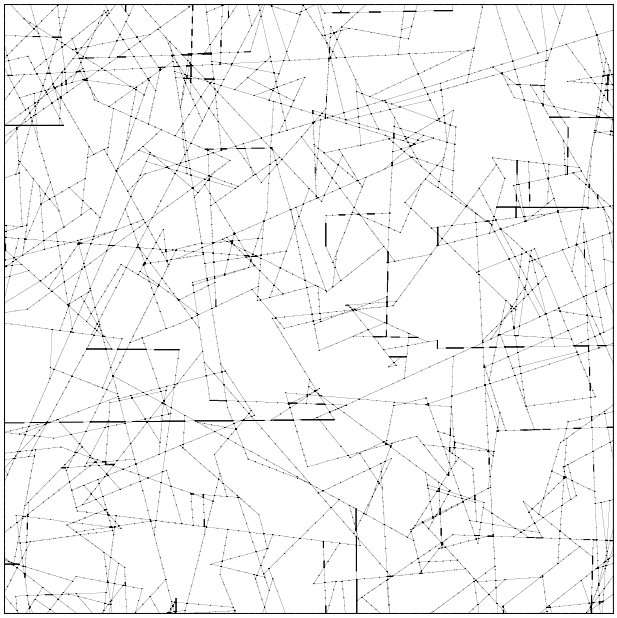

Fig. 12. Geometry of fracture system in the DFN model

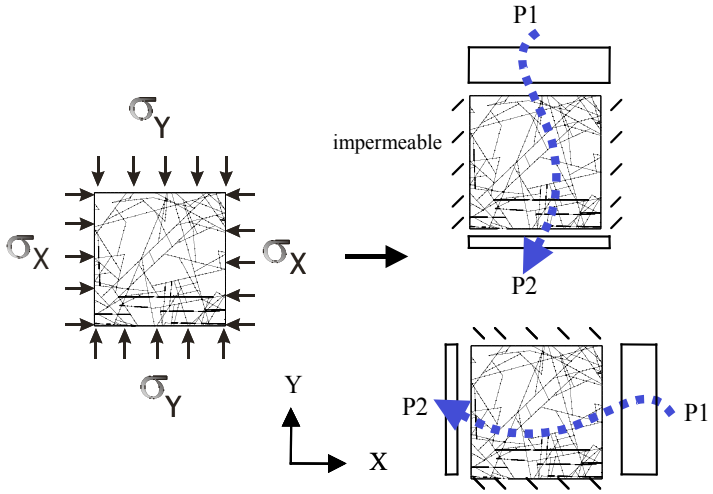

Fig. 13. Applications of stress boundary conditions and calculation of equivalent permeability in the x- and y-directions. σ_x and σ_y indicate the boundary stresses applied in horizontal and vertical directions, respectively. P1 and P2 indicate the hydraulic pressure applied in the boundaries, with P1 larger than P2.

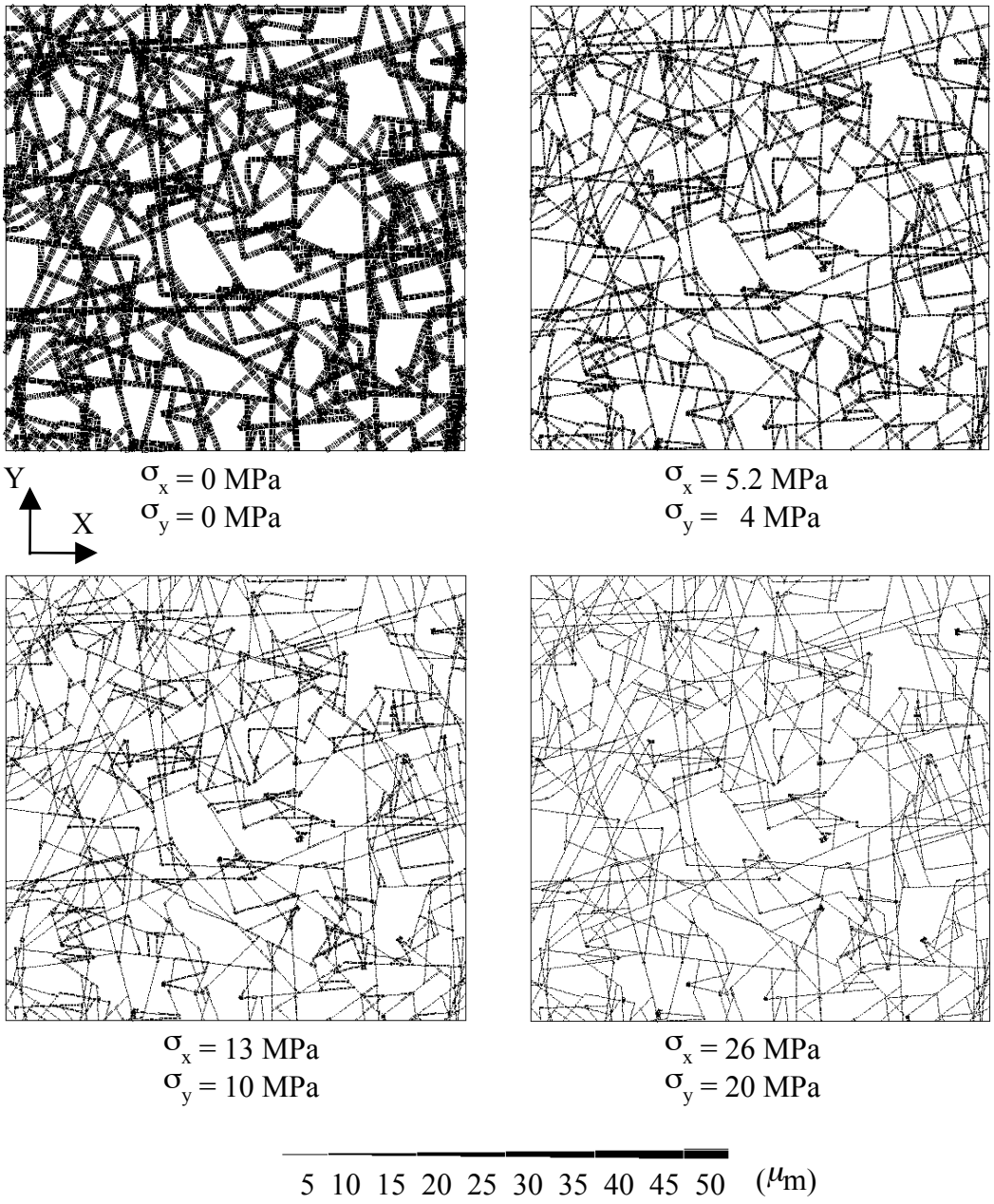

Fig. 14. Change of fracture apertures with the increase of stresses for the fixed stress ratio of 1.3. The thickness of lines indicates the magnitude of apertures. Mean apertures for the four cases were 30, 16.8, 11.9, and 8.8 μm, respectively.

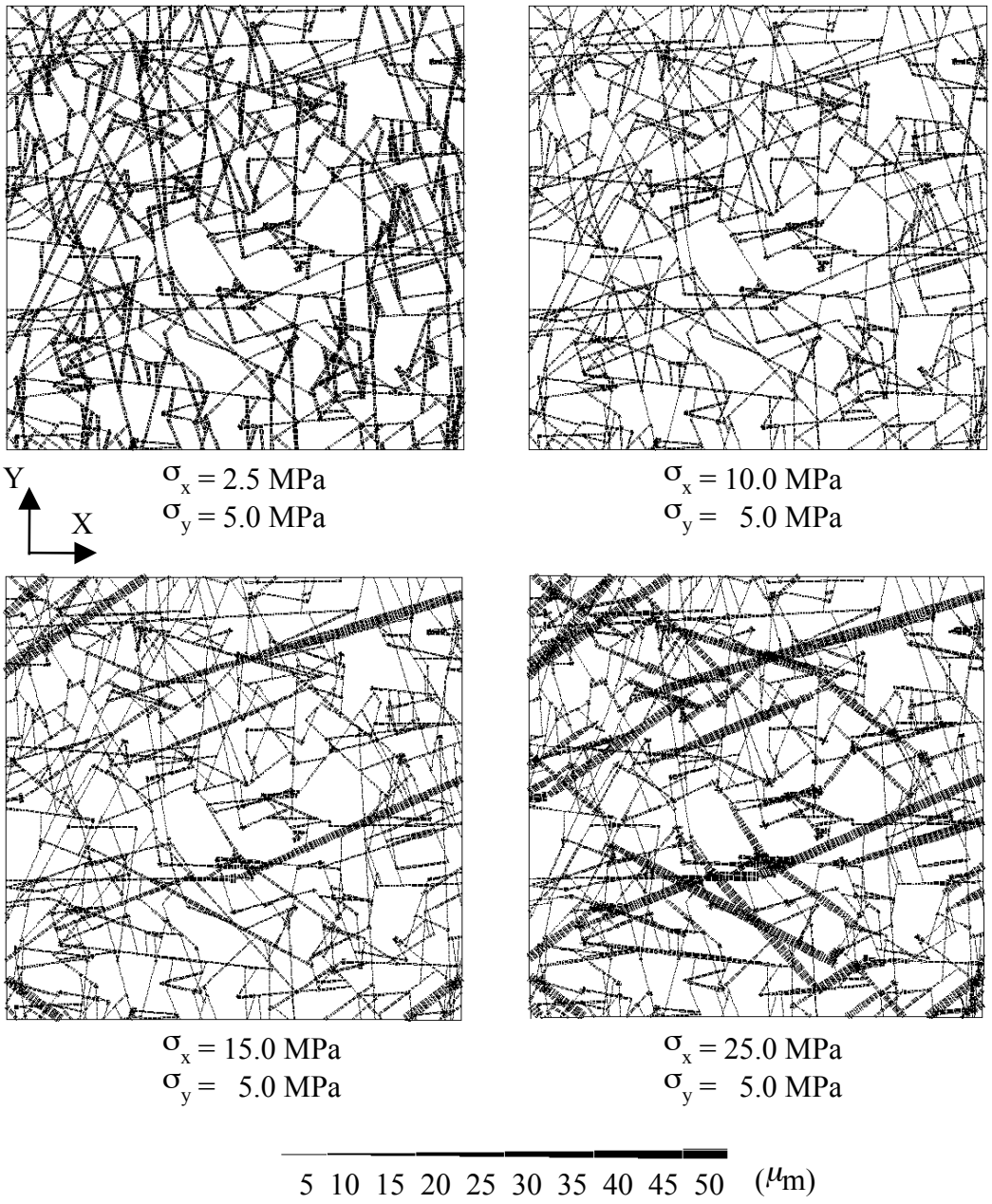

Fig. 15. Changes in fracture apertures with the increase in stress ratio, with the fixed vertical stress = 5 MPa. The thickness of the line indicates the magnitude of apertures.

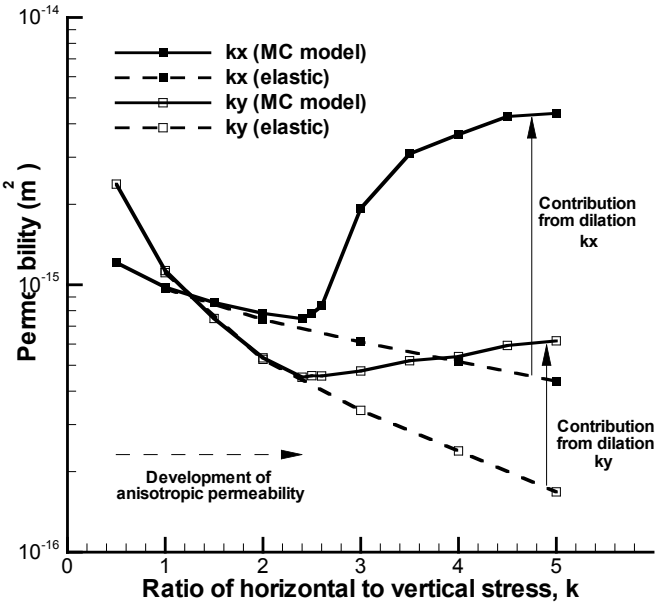

Fig. 16. Equivalent permeability (k_x and k_y) change due to the change in stress ratio. Differential stress is increased while keeping the magnitude of vertical stress constant. Mohr Coulomb (MC) model (solid lines) is compared with the pure elastic model with no shear failure (dashed lines).

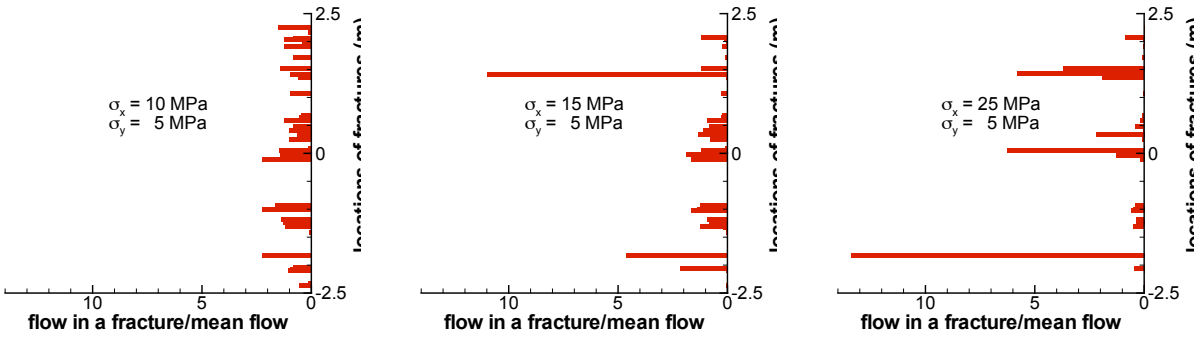

Fig. 17. Normalized flow rates at the left vertical boundary of the model at points where the boundary is intercepted by fractures. The three subfigures show the normalized flow rates for stress ratios of 2, 3, and 5 respectively.

Hydromechanical Effects Involved in CO_2 Injection and Storage

Disposal or storage of pressurized CO_2 from fossil-fired power plants in deep saline aquifers has been suggested as one of the promising concepts for reducing emission of greenhouse gases into the atmosphere (DOE 1999). The injection would take place at a depth below 800 m, so that the CO_2 would be within the temperature and pressure range for it to be a supercritical fluid. As a supercritical fluid, the CO_2 behaves like a gas with low viscosity, but with a liquid-like density approximately half that of the formation brine, depending on pressure and temperature. Thus, large volumes of CO_2 gas would be compressed to a higher-density supercritical fluid and stored in a much smaller volume in the brine formation.

In this section, caprock mechanical and HM changes are studied during CO_2 injection into a hypothetical sandstone aquifer covered by semipermeable shale (Rutqvist & Tsang 2005). The problem is analyzed using the coupled computer codes TOUGH2-FLAC3D (Rutqvist *et al.* 2002), which simulate multiphase flow—in this case supercritical CO_2, water and salt—coupled with heat transfer and rock deformation.

For general discussion,, it is useful to consider a basic injection-and-storage scenario and storage of CO_2 in brine formations, as presented in Fig. 18, which shows a storage injection zone overlain by a caprock greater than 800 m in depth. Three main physico-chemical processes are indicated. First, we note the hydrological process of CO_2 buoyancy flow, with its factor-of-two lower density and an order-of-magnitude lower viscosity. Thus, by buoyancy, the plume of injected CO_2 will migrate outwards from the injection well and upwards towards the caprock. Other hydrologic factors also come into play, which will be discussed below. Second, both injection and buoyancy provide additional pressure on the rock matrix of the formation, which may thus be deformed, with changes in matrix porosity or fracture apertures. They in turn cause changes in flow permeability and, consequently, the flow field. Finally, the injected CO_2 plume will, in general, chemically react with the formation minerals. This could give rise to porosity changes near the injection well, but, positively, such chemical changes can react with the injected CO_2 to form new minerals in the rock matrix, thus trapping CO_2 chemically. This is the mineral trapping process for sequestration of CO_2.

Because supercritical CO_2 is less dense than water, deep underground disposal requires a sufficiently impermeable seal (caprock) above an underground storage zone in order to trap the injected CO_2. However, disposal from one standard-size 1,000 MW coal-fired power plant for 30 years could occupy more than 100 km^2 of a 100 m thick zone (Pruess *et al.* 2001). Over such a vast area, it is not likely that we would find a caprock that is perfectly homogeneous and impermeable (Fig. 19). A caprock may be discontinuous and may contain imperfections such as faults and fractures of various sizes (from small meter-scale fractures to kilometer-scale faults). Further, the hydraulic properties of a fault may change with injection-induced hydraulic pressure. Thus, the performance assessment of CO_2 storage in an underground brine formation requires the analysis of a number of simultaneously interacting processes, including multiphase flow, heat transfer, and mechanical deformation. Rock deformation and stresses are important because the injection of CO_2, in general, produces an increased pore pressure, which in turn will change the stress field and cause deformations in the rock mass (Fig. 19). Changes in the stress field can affect the performance of an injection site in several ways. First, if sufficiently large, they could cause failure, giving rise to a high-permeability leakage path through fractured rock. Secondly, the induced stresses will act upon pre-existing faults and fractures, and cause opening or slip displacement with associated permeability changes. Such hydromechanical changes in a caprock could damage the sealing characteristics for a safe long-term containment of the CO_2. Thirdly, it is well known that extraction of fluid from an underground reservoir (for example, oil and gas) causes subsidence of the ground surface. By the same processes,

an underground injection of compressed CO_2 can cause the ground surface to heave (uplift) because of a reduction in effective stress in the aquifer.

Fig. 20 presents the injection pressure during a 30-year period with or without consideration of the stress-dependent rock-mass permeability. At constant injection rate, the injection pressure increases continuously during the injection and tends to 37 or 43 MPa, depending on whether stress-dependent permeability changes are considered. The difference in peak pressure is explained by the fact that the permeability in the injection zone in the former case increases because of a general reduction in effective stresses during injection. Thus, the stress-dependent permeability changes in the aquifer would have a positive effect on the CO_2 injection operation, because a higher flow rate can be maintained without increasing the injection pressure over the lithostatic pressure for a longer time. In this modeling, the injection pressure would exceed the lithostatic pressure (or the minimum compressive principal stress) after about 10 years of injection. Because we are not modeling the nonlinear stress-deformation behavior of hydraulic fracturing or plastic shear, our calculations will be performed for up to 10 years of injection. In practice, the injection rate would be reduced after a number of years to ensure that the injection pressure is not close to the lithostatic value.

Coupled HM interactions in a caprock/reservoir system are studied with a view towards evaluating the integrity of the caprock system and reservoir leakage. We will analyze the possibilities of caprock failure by looking at the critical pressure that could induce hydraulic fracturing or the critical pressure that could induce shear slip of pre-existing faults. A conservative assumption is that a hydraulic fracture could develop as soon as the fluid pressure exceeds the least compressive principal stress, and hence, the critical pressure for fracturing is:

$$P_{fc} = -\sigma_3 \tag{6}$$

We define a pressure margin to the onset of hydraulic fracturing as

$$P_{fm} = P - P_{fc} < 0 \tag{7}$$

which should be kept negative to prevent fracturing. Thus, P_{fm} tells us how much further the pressure can be increased before fracturing is initiated.

A conservative assumption for the onset of fault slip is to assume that a fault could exist at any point and have any orientation. For such a case, the Columb failure criteria can be written in the following form:

$$\tau_{m2} = \left(\sigma_{m2} - P\right)\sin\phi + S_0\cos\phi \tag{8}$$

where τ_{m2} and σ_{m2} are the two-dimensional maximum shear stress and mean stress in the plane σ_1, σ_3, respectively, and are defined as:

$$\tau_{m2} = \frac{1}{2}\left(\sigma_1 - \sigma_3\right) \tag{9}$$

$$\sigma_{m2} = \frac{1}{2}\left(\sigma_1 + \sigma_3\right) \tag{10}$$

and S_0 and ϕ are the fault's coefficient of internal cohesion and angle of internal friction, respectively.

In analogy with the criterion for hydraulic fracturing, we can define the critical pressure for the onset of slip as:

$$P_{sc} = \sigma_{m2} + S_0 \cot\phi - \frac{\tau_{m2}}{\sin\phi} \tag{11}$$

For faults, a zero cohesion may be assumed and a typical range for ϕ is 25° to 35°. In this calculation, we test for slip using a zero cohesion and a friction angle of 30°, leading to the following pressure margin for the onset of slip:

$$P_{sm} = P - P_{sc} < 0 \tag{12}$$

Figs. 21 and 22 show the zones of possible fault slip and hydraulic fracturing for two different stress regimes, defined in terms of the relationship between the horizontal and vertical stresses (σ_h and σ_v respectively):

- An isotropic stress regime ($\sigma_h = \sigma_v$);
- A normal fault stress regime ($\sigma_h = 0.7\sigma_v$).

In these figures, the potential for hydraulic fracturing and for fault slip were evaluated using Equations (7) and (12). For the isotropic stress regime, mechanical failure would most likely initiate at the interface between the caprock and injection zone, where the reduction in vertical effective stress can lead to the formation of horizontal hydraulic fractures (Fig. 21, lower part). Furthermore, a larger zone of possible slip on pre-existing fractures occurs at the upper and lower part of the injection zone (Fig. 21, upper). This implies that an unfavorably oriented fault could be reactivated with possible permeability change. However, even if fracturing or fault reactivation were to take place in the lower part of the caprock, the simulation indicates that reactivation would be contained within this area and not propagate through the upper part of the cap.

Fig. 22 shows that, for the normal faulting stress regime, the zones of potential shear slip and hydraulic fracturing are more extensive. This is because in this case, the initial, far-field horizontal stress is lower. Importantly, in the case of a normal faulting stress regime, shear slip and hydraulic fracturing would preferentially occur on vertical fractures. Further, the shear slip could occur in the entire caprock and not just in its lower part. In other words, there is a potential for slip on a pre-existing fault crossing the entire caprock, and hence CO_2 leakage along it.

As a general presentation of coupled hydromechanical changes during a CO_2 disposal operation, the present analysis is somewhat simplified, and the results should be taken only qualitatively for any particular site, because quantitative results are very sensitive to local rock properties. At a real injection site, the parameters for these empirical relationships should be calibrated against *in situ* measurements at an appropriate scale and over an appropriate range of conditions.

Overall, the analysis shows that the magnitude and the anisotropy of the initial stress field is an important factor in determining where and how failure could occur. In the case of an isotropic stress field, with both stresses equal to the weight of the overburden, shear slip along low-angle faults and the formation of horizontal hydraulic fractures are the most likely failure modes. In the case of relatively low horizontal stress (the normal fault stress regime, which might be the most common case in storage formations), shear slip along steep faults and formation of vertical fractures are the most likely failure modes.

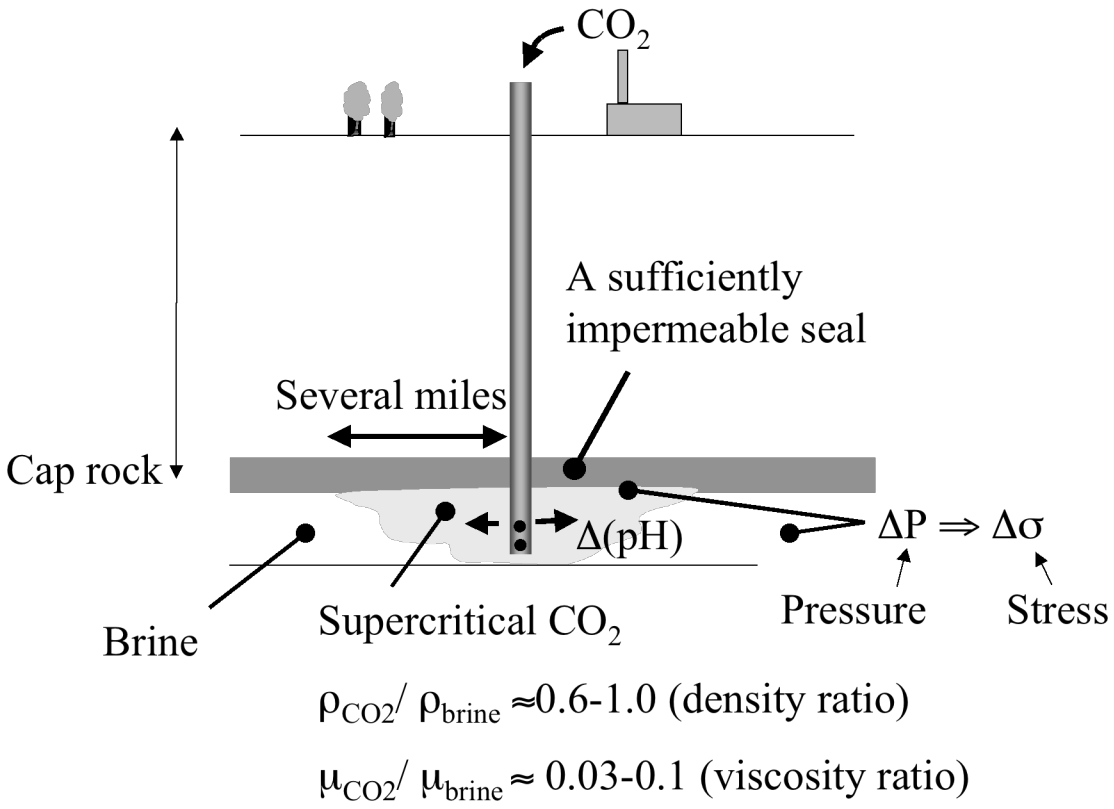

Fig. 18. A basic scenario for CO_2 injection and storage in a brine formation

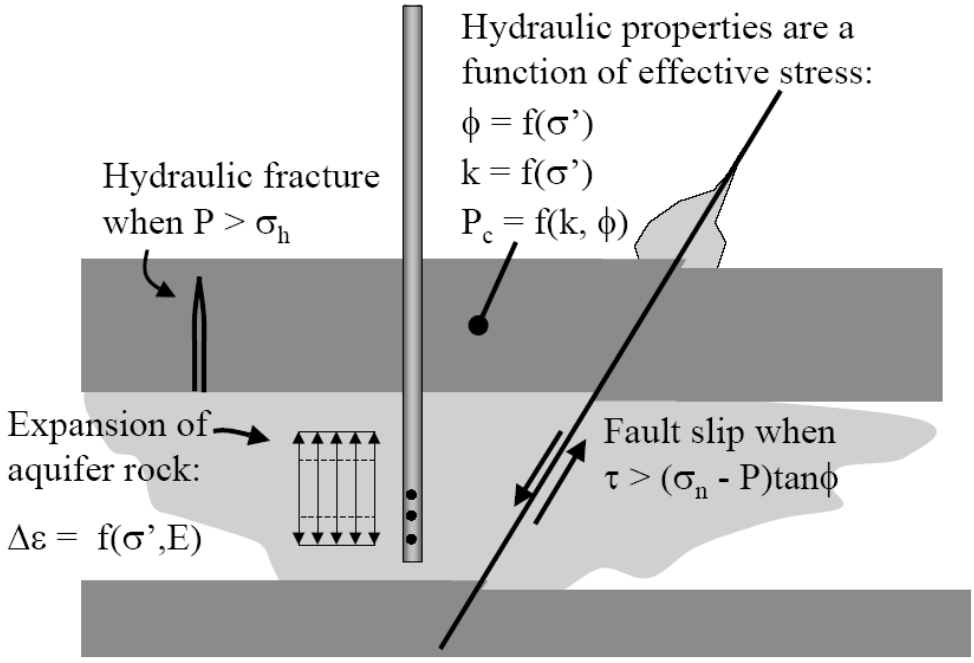

Fig. 19. Hydromechanical processes associated with CO_2 injection. Here, ϕ is the porosity of the caprock.

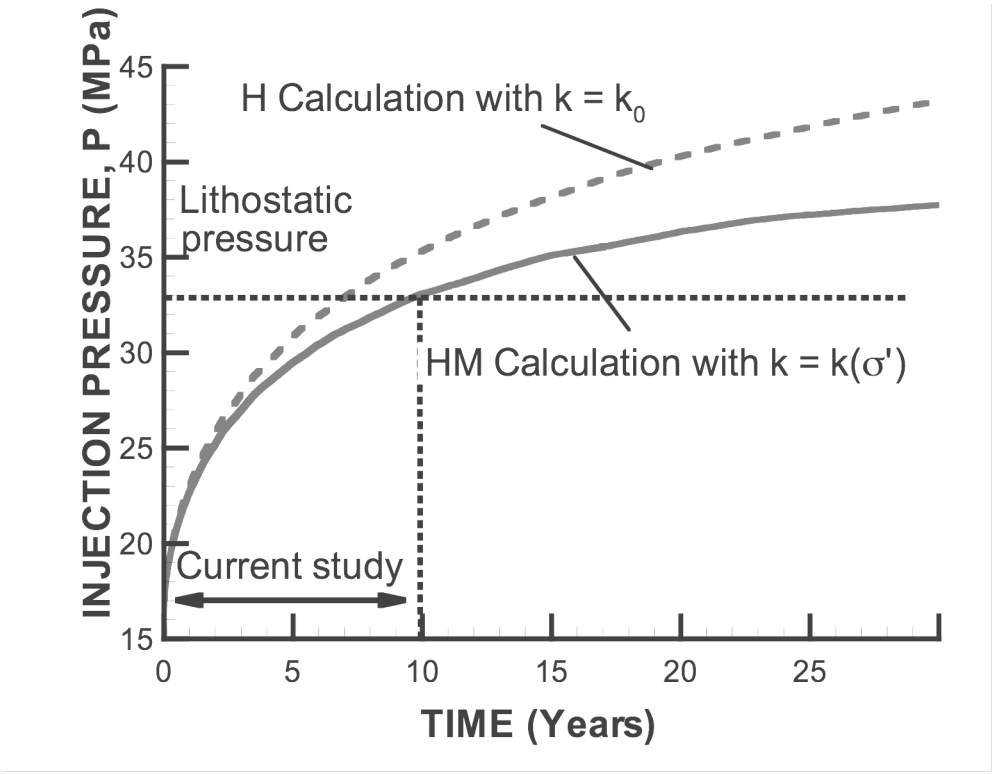

Fig. 20. Injection pressure as a function of time

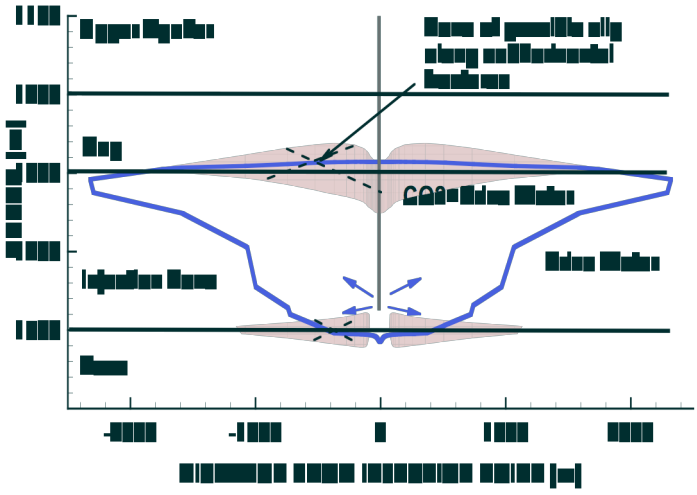

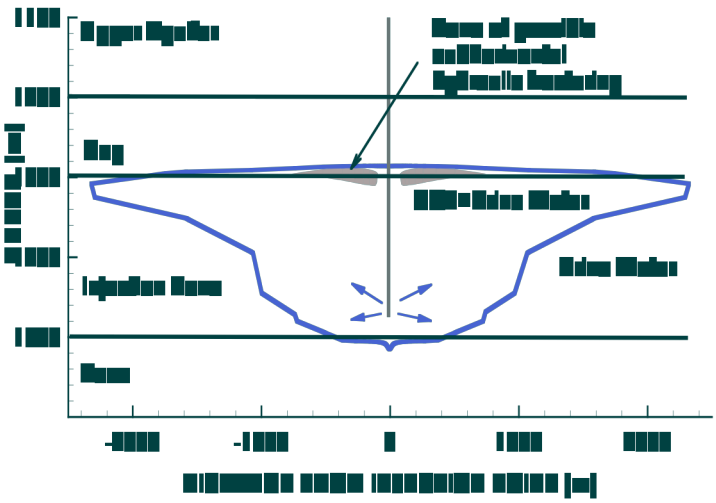

Fig. 21. Calculated zones of possible shear slip (upper plot) and hydraulic fracturing (lower plot) after 10 years of injection for the case of isotropic stress regime ($\sigma_h = \sigma_v$).

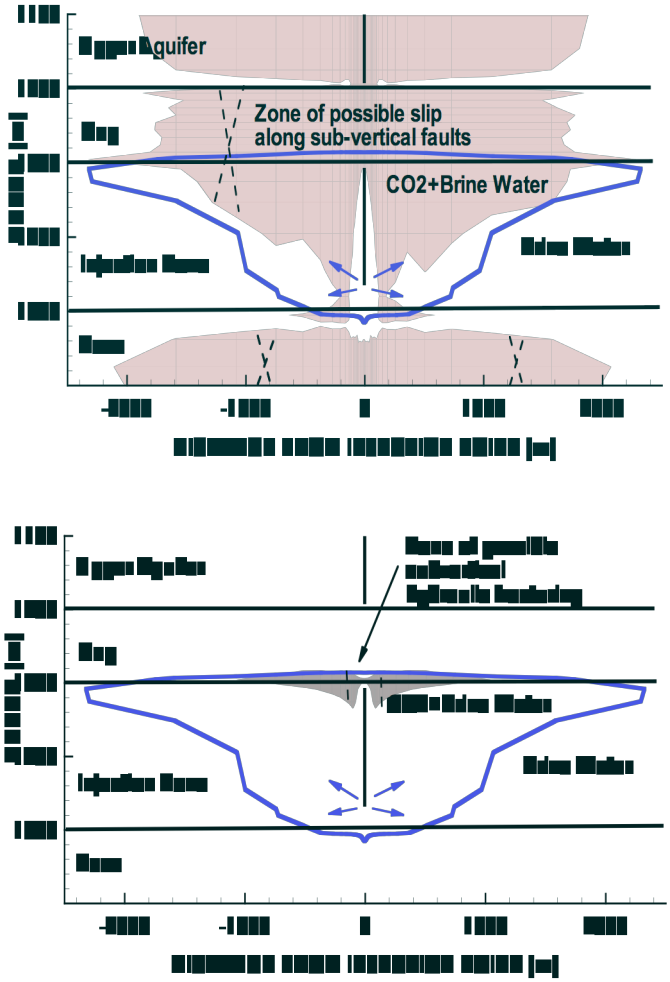

Fig. 22. Calculated zones of possible shear slip (upper plot) and hydraulic fracturing (lower plot) after 10 years of injection for the case of a normal faulting stress regime ($\sigma_h = 0.7\sigma_v$)

The study was extended to include injection into a reservoir/caprock system bounded by two sealing faults. Fig. 23 shows an example of fault reactivation analysis using this model. In this example, CO_2 is injected within a permeable injection zone laterally confined between two sealing (low-permeability) faults. An internal friction angle of 25° is assumed for the faults. In this case, CO_2 was injected at high pressure until slip was triggered along the two bounding faults. A maximum fault slip of about 5 cm was predicted along fault sections intersecting the injection zone (Fig. 23, right). However, analysis shows that shear failure is limited to a zone of substantially increased fluid pressure and does not propagate further than about 100 m above and below the injection zone. In general, the stress evolution around the faults and the injection zone is more complex in this case than for the homogenous caprock case. Localized concentration of stresses (including shear stresses), as well as localized stress releases, is more likely, and this could lead to additional damage, particularly in areas where the fault intersects the caprock. Such damage may induce increased permeability along the fault. However, this possibility was not considered in this initial study.

In general, slip on pre-existing faults and other discontinuities intersecting the caprock are viewed as a likely scenario for generation of possible CO_2 leakage paths. However, further analysis is required to evaluate whether fluid flow will occur in conjunction with the slip. Shear tests on single fractures in shale indicate that permeability can increase or decrease depending on the current stress normal to the fractures (Gutierrez *et al.* 2000). At high normal stresses, shear slip is accompanied with significant gouge production, and the permeability can actually decrease by several orders of magnitude. However, geological studies indicate that local stresses and the presence of faults control containment and release of deep overpressured fluids. Further research is needed for a realistic modeling of complex fault structures and for modeling of potential changes in fault permeability and mechanical properties.

In summary, the following points on coupled hydromechanical effects in CO_2 injection may be emphasized:

- A general reduction in the effective mean stress induces strongly coupled hydromechanical changes in the lower part of the caprock. Therefore, the strongest hydromechanical changes and the greatest risk of rock failure occur in the lower part of the caprock.
- Because the aquifer pressure slowly increases during the injection period, fluid has time to diffuse into the rock and create horizontal poroelastic stresses. These events will decrease the probability of fracturing and shear of subvertical fractures, but also make the shear reactivation along subhorizontal fracturesmore likely. Thus, shear reactivation of existing fractures is the primary failure mode of concern in CO_2 injection.
- The analysis indicates that shear reactivation in the lower part of the caprock could take place at an injection pressure well below the lithostatic pressure. However, depending on the initial *in situ* stress field, this fault slip reactivation may or may not be confined to the lower parts of the caprock.
- The type of stress regime (e.g., isotropic or normal fault types) is a key parameter that determines whether fracturing and shear slip are likely to take place along subhorizontal or subvertical fractures. For a common normal fault type of stress regime, fracture slip would preferentially take place along subvertical fractures, so that hydraulic fracturing would be vertical.
- Once the CO_2 fluid reaches the upper part of the caprock (for example, through a permeable fault), the upward CO_2 migration is accelerated because of the combined effects of relative permeability and viscosity changes, and changes in intrinsic permeability caused by pressure-induced hydromechanical effects.

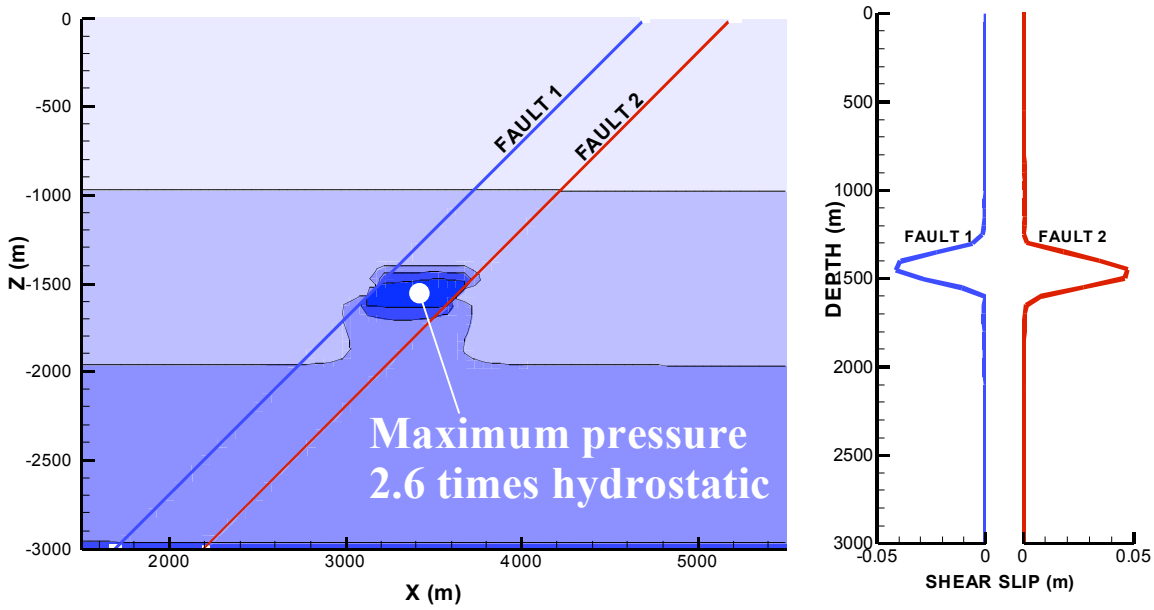

Fig. 23. Fault slip during CO_2 injection. Right figure shows contours of fluid pressure; left figure shows the magnitude of shear displacement along faults 1 and 2.

Concluding Remarks

Fractured rock hydromechanics is a rich field of research, as exemplified by the four studies described in some detail above. These studies demonstrate the intricate interactions and couplings of hydrologic and mechanical effects in four very different problems. The results of these problems have significant implications for practical issues of interest to society, such as contaminant transport, tunnel stability, sequestration of greenhouse gases, and site characterization of a geological system.

There are a number of outstanding challenges in this field. They include the following:

- *Hydromechanical effects involving multiple fractures and faults.* Except for the first study, the examples covered in this paper all require, to varying degrees, the consideration of the interference among neighboring fractures or faults in order to understand the hydromechanical behavior of the system. More field and modeling investigations are needed on such multifracture systems.
- *Constitutive relationships and equations of state.* In the discussions within this paper, we have assumed that the constitutive relationships for mechanical processes and the equations of state of fluids are available for modeling studies. While much information is available, the state-of-art is still lacking for shear-processes on certain rock materials and for certain fluid mixtures.
- *Hydromechanical processes for a broad range of space and time scales.* The concern is how to relate the pore-scale behavior all the way up to the basin scale, and similarly how to relate the time scale of a typical field or laboratory experiment to that of the natural geological system. For this, knowledge of, and treatment techniques for, heterogeneities in geological media are very much needed.

- *Key parameters from site characterization.* All problems of practical importance concern a site, and how to obtain key parameters associated with hydromechanical processes at the site is still very much an open problem. Definition of these key parameters depends on the issues of concern for the site. Research is needed not only on new site measurement techniques, but also on modeling methods that integrate the data and reflect an understanding of how these data relate to the parameters that are key to the issues.

Acknowledgments

The authors would like to thank many collaborators over the years on studies described in this paper. In particular they would like to acknowledge helpful discussions with members of the DECOVALEX project, especially with Ove Stephansson, John Hudson, and Lanru Jing. The paper was prepared with partial support of the U.S. Department of Energy under Contract No. DE-AC02-05CH11231 with the Lawrence Berkeley National Laboratory.

References

Andersson, J., & Knight, L. 2000. DECOVALEX III Project, TASK 3, BMT2 protocol, Understanding the impact of upscaling THM processes on performance assessment. Version 6.0, Swedish Nuclear Power Inspectorate, Stockholm, Sweden.

Biot, M.A. 1941. General theory of three-dimensional consolidation. *J. Applied Physics*, **12**, 155–164.

DOE, 1999. Carbon sequestration research and development, D. Reichle and others (eds.), *U.S. Department of Energy Report DOE/SC/FE-1*, Washington, DC.

Gutierrez, M., Oino, L.E., & Nygård, R. 2000. Stress-dependent permeability of a de-mineralised fracture in shale. *Marine and Petroleum Geology*, **17**, 895–907.

Ekman, D. 1997. *Rock stress, hydraulic conductivity and stiffness of fracture zones in the Laxemar Borehole, Småland, Sweden.* Masters Thesis. Division of Engineering Geology, Royal Institute of Technology, Sweden.

Itasca Consulting Group, 1997. FLAC 3D, Fast Lagrangian Analysis of Continua in 3 Dimensions. Version 2.0. Five volumes. Minneapolis, Minnesota: Itasca Consulting Group.

Jing, L., & Hudson, J.A. 2002. Numerical methods in rock mechanics. *Int J Rock Mech Mining Sci*., **39**, 409-427

Lee, C.I., & Chang, K.M. 1995. Analysis of permeability change and groundwater flow around underground oil storage cavern in Korea. *Proceedings of the Eighth ISRM Congress*, Tokyo, Japan. Rotterdam: Balkema, pp. 779–782.

Londe, P., & Sabarly, F. 1966, La distribution des perméabilitésdans la fondation des barrages voûtes en fonction du champ de contrainte. In: *Proc 1st International Congress on Rock Mechanics*, Lisbon, Vol II, pp. 517–522.

Louis, C., Dessenne, J.-L. & Feuga, B. 1977, Interaction between water flow phenomena and the mechanical behavior of soil or rock masses. In: Gudehus, G. (ed), *Finite Elements in Geomechanics*. John Wiley & Sons, pp. 479–511.

McKinley, L., Kickaier, W., del Olmo, C., & Huertas, F. 1996. The FEBEX Project: Full-scale simulation of engineered barriers for a HLW repository. *NAGRA Bulletin No 27*, NAGRA, Switzerland.

Min, K.B., & Jing, L. 2003. Numerical determination of the equivalent elastic compliance tensor for fractured rock masses using the distinct element method. *Int J Rock Mech Min Sci*, **40**(6), 795–816.

Min, K.B., Rutqvist, J., Tsang, C.-F., & Jing, L. 2003. A block-scale stress-permeability relationship of fractured rock determined by numerical experiments, In: Stephansson O, Hudson JA, Jing L (eds), *Proceedings of Int Conf on Coupled T-H-M-C Processes in Geosystems: GeoProc 2003*, Stockholm, 257–262.

Min, K.B., Rutqvist, J., Tsang, C.-F., & Jing, L. 2004. Stress-dependent permeability of fracture rock masses: a numerical study. *Int. J. Rock Mech. & Min. Sci*, **41**, 1191–1210.

Noorishad, J., Ayatollahi, M.S., & Witherspoon, P.A. 1982. A finite element method for coupled stress and fluid flow analysis of fractured rocks. *Int. J. Rock Mech. Min. Sci. & Geomech. Abstr.*, **19**, 185–193.

Noorishad, J., & Tsang, C.-F. 1996. Coupled thermohydroelasticity phenomena in variable saturated fractured porous rocks—Formulation and numerical solution. In Stephansson, O., Jing, L., and Tsang, C.-F. editors. *Coupled Thermo-Hydro-Mechanical Processes of Fractured Media. Developments in Geotechnical Engineering*, Elsevier, 79, pp. 93–134.

Noorishad, J., Tsang, C.-F., & Witherspoon, P.A. 1984. Coupled thermal-hydraulic-mechanical phenomena in saturated fractured porous rocks: numerical approach. *J. Geophys. Res.,* **89**, 10365–10373.

Noorishad, J., Tsang, C.-F., & Witherspoon, P.A. 1992. Theoretical and field studies of coupled hydromechanical behavior of fractured rocks 1. Development and verification of a numerical simulator. *International Journal of Rock Mechanics and Mining Sciences, 29,* (4) 401-409.

Pahl, A., Heussermann, St., Bräuer, V., & Gloggler, W. 1989. Grimsel Test Site. Rock stress investigations. *NAGRA*, NTB, 88-39E.

Pruess, K., Oldenburg, C., & Moridis, G. 1999. TOUGH2 User's Guide, Version 2.0, Lawrence Berkeley National Laboratory *Report LBNL-43134*, Berkeley, CA.

Pruess, K., Xu, T., Apps, J. & Garcia, J. 2001. Numerical modeling of aquifer disposal of CO_2. *Society of Petroleum Engineers, SPE Paper No. 66537*.

Renshaw, C.E., & Park, J.C. 1997. Effect of mechanical interactions on the scaling of fracture length and aperture. *Nature*, **386**, 482–484.

Rutqvist, J. 1995. Determination of hydraulic normal stiffness of fractures in hard rock from hydraulic well testing. *Int. J. Rock Mech. Min. Sci. & Geomech. Abstr*, **32**, 513–523.

Rutqvist, J., Börgesson, L., Chijimatsu, M., Kobayashi, A., Nguyen, T.S., Jing, L., Noorishad, J., & Tsang, C.-F. 2001. Thermohydromechanics of partially saturated geological media—Governing equations and formulation of four finite element models. *Int. J. Rock Mech. & Min. Sci.*, **38**, 105–127.

Rutqvist, J., Rejeb, A., Tijani, M., & Tsang, C.F. 2004. Analyses of coupled hydrological-mechanical effects during drilling of the FEBEX tunnel at Grimsel. In: Stephansson, O., Hudson, J.A., & Jing, L., eds., *Coupled T-H-M-C Processes in Geo-Systems: Fundamentals, Modelling,*

Experiments and Applications. Elsevier Geo-Engineering Book Series, Volume 2, Oxford, p. 131–136, 2004.

Rutqvist, J., & Stephansson, O. 2003. The role of hydromechanical coupling in fractured rock engineering. *Hydrogeology Journal*, **11**, 7–40.

Rutqvist, J., & Tsang, C.F. 2005. Coupled hydromechanical effects in CO_2 injection. In: Developments in Water Science, **52**. *Underground Injection Science and Technology*, C.F. Tsang and J.A. Apps, Editors, Elsevier Science Publishers, pp. 651–680.

Rutqvist, J., Tsang, C-F, Ekman, D., & Stephansson, O. 1997. Evaluation of *in situ* hydromechanical properties of rock fractures at Laxemar in Sweden. In *Proc 1st Asian Rock Mechanics Symposium ARMS 97*, Seoul, Korea, pp. 619–624.

Rutqvist, J., Wu, Y.-S., Tsang, C.-F., & Bodvarsson, G.S. 2002. A modeling approach for analysis of coupled multiphase fluid flow, heat transfer, and deformation in fractured porous rock. *Int. J. Rock Mech. & Min. Sci.* **39**, 429–442.

Tsang, C.-F., ed., 1987. *Coupled Processes Associated with Nuclear Waste Repositories*, Academic Press.

Tsang, C.-F. 1991. Coupled thermomechanical hydrochemical processes in rock fractures. *Review of Geophysics*, **29**(4), 537–551.

Tsang, C.-F. 1999. Linking thermal, hydrological and mechanical processes in fractured rocks. *Annual Review of Earth and Planetary Sciences*, **27**, 359–384.

Figure Captions:

Fig. 1. TOUGH-FLAC simulator coupled THM analysis with multiphase fluid flow

Fig. 2. *In situ* determination of hydromechanical properties of rock joints

Fig. 3. Hydraulic jacking test: pressure and flow-rate data

Fig. 4. Schematic picture of pressure profiles in a fractured rock during a hydraulic jacking test and a pulse injection test

Fig. 5. Numerical modeling and field experiment data for a hydraulic-jacking test involving increasing and then decreasing pressure steps. For comparison, the expected result for a rigid fracture is shown as the broken line.

Fig. 6. During TBM excavation of the FEBEX tunnel, distinct increases in fluid pressure were observed in a borehole interval (P4) located a few meters away from the drift wall (from McKinley *et al.* 1996).

Fig. 7. Mesh design for simulating stress and pore-pressure changes around the FEBEX tunnel

Fig. 8. Calculated changes in mean stress at the end of the second step of excavating the FEBEX tunnel (see Fig. 6, 61 m on the right axis)

Fig. 9. Calculated change in pore pressure at the end of the second step in excavating the FEBEX tunnel (see Fig. 6, 61 m on the right axis)

Fig. 10. Predicted and measured pore-pressure evolution for the estimated regional stress field

Fig. 11. Simulated and measured pore-pressure evolution for the adjusted local stress field

Fig. 12. Geometry of fracture system in the DFN model

Fig. 13. Applications of stress boundary conditions and calculation of equivalent permeability in the x- and y-directions. σ_x and σ_y indicate the boundary stresses applied in horizontal and vertical directions, respectively. P1 and P2 indicate the hydraulic pressure applied in the boundaries, with P1 larger than P2.

Fig. 14. Change of fracture apertures with the increase of stresses for the fixed stress ratio of 1.3. The thickness of lines indicates the magnitude of apertures. Mean apertures for the four cases were 30, 16.8, 11.9, and 8.8 μm, respectively.

Fig. 15. Changes in fracture apertures with the increase in stress ratio, with the fixed vertical stress = 5 MPa. The thickness of the line indicates the magnitude of apertures.

Fig. 16. Equivalent permeability (k_x and k_y) change due to the change in stress ratio. Differential stress is increased while keeping the magnitude of vertical stress constant. Mohr Coulomb (MC) model (solid lines) is compared with the pure elastic model with no shear failure (dashed lines).

Fig. 17. Normalized flow rates at the left vertical boundary of the model at points where the boundary is intercepted by fractures. The three subfigures show the normalized flow rates for stress ratios of 2, 3, and 5 respectively.

Fig. 18. A basic scenario for CO_2 injection and storage in a brine formation

Fig. 19. Hydromechanical processes associated with CO_2 injection. Here, ϕ is the porosity of the caprock.

Fig. 20. Injection pressure as a function of time

Fig. 21. Calculated zones of possible shear slip (upper plot) and hydraulic fracturing (lower plot) after 10 years of injection for the case of isotropic stress regime ($\sigma_h = \sigma_v$)

Fig. 22. Calculated zones of possible shear slip (upper plot) and hydraulic fracturing (lower plot) after 10 years of injection for the case of normal faulting stress regime ($\sigma_h = 0.7\sigma_v$)

Fig. 23. Fault slip during CO_2 injection. Right figure shows contours of fluid pressure; left figure shows the magnitude of shear displacement along faults 1 and 2.